

Gravity wave breaking in two and three dimensions

1. Model description and comparison of two-dimensional evolutions

Øyvind Andreassen and Carl Erik Wasberg

Norwegian Defense Research Establishment, Kjeller

David C. Fritts and Joseph R. Isler

Laboratory for Atmospheric and Space Physics and
Department of Electrical and Computer Engineering University of Colorado, Boulder

Abstract. A nonlinear, compressible, spectral collocation code is employed to examine gravity wave breaking in two and three spatial dimensions. Two-dimensional results exhibit a structure consistent with previous efforts and suggest wave instability occurs via convective rolls aligned normal to the gravity wave motion (uniform in the spanwise direction). Three-dimensional results demonstrate, in contrast, that the preferred mode of instability is a series of counterrotating vortices oriented along the gravity wave motion, elongated in the streamwise direction, and confined to the region of convective instability within the wave field. Comparison of the two-dimensional results (averaged spanwise) for both two- and three-dimensional simulations reveals that vortex generation contributes to much more rapid wave field evolution and decay, with rapid restoration of near-adiabatic lapse rates and stronger constraints on wave energy and momentum fluxes. These results also demonstrate that two-dimensional models are unable to describe properly the physics or the consequences of the wave breaking process, at least for the flow parameters examined in this study. The evolution and structure of the three-dimensional instability, its influences on the gravity wave field, and the subsequent transition to quasi-isotropic small-scale motions are the subjects of companion papers by Fritts et al. (this issue) and Isler et al. (this issue).

Introduction

Atmospheric gravity waves were first studied in connection with airflow over orography and atmospheric fluctuations at greater altitudes several decades ago. More recently, they have enjoyed a resurgence of interest with the recognition of their major role in the transports of energy and momentum throughout the atmosphere. This interest has focused on the wave-wave and wave-mean flow interactions accompanying wave propagation as well as the processes acting to limit wave amplitudes and control their spectral character. An important component of this latter work was the attempt to understand the effects of wave field instability on wave amplitudes, turbulent diffusion, and the convergences of wave energy and momentum fluxes accompanying dissipation.

Initial studies addressed the potential for gravity wave momentum transports and their effects due to wave dissipation [Bretherton, 1969; Holton and Lindzen,

1972]. These efforts were extended as our understanding of gravity wave transports and filtering improved [Holton, 1982; Dunkerton, 1982; Garcia and Solomon, 1985; Palmer et al., 1986; McFarlane, 1987; McIntyre, 1989]. Other studies examined wave structure, evolution, and dissipation near a critical level [Hazel, 1967; Fritts, 1979, 1982; Winters and D'Asaro, 1989; Dunkerton and Robins, 1992] or the more general evolution of a gravity wave increasing in amplitude as density decreases [Fritts, 1985; Dunkerton, 1987; Walterscheid and Schubert, 1990; Huang et al., 1992]. In all these studies, however, wave propagation and instability were assumed to be two-dimensional (2-D), with all motions confined to the plane of wave propagation. Only more recently have gravity wave studies included consideration of three-dimensional (3-D) effects and instability structures in atmospheric and oceanic applications [Clark and Farley, 1984; Winters and Riley, 1992; Winters and D'Asaro, 1993].

There is, nevertheless, extensive literature on 3-D instability and transition to 3-D structure in free shear or convective layers which has relevance to our simulations. Evidence of streamwise vortex structures occurring in the presence of spanwise uniform Kelvin-

Copyright 1994 by the American Geophysical Union.

Paper number 93JD03435.
0148-0227/94/93JD-03435\$05.00

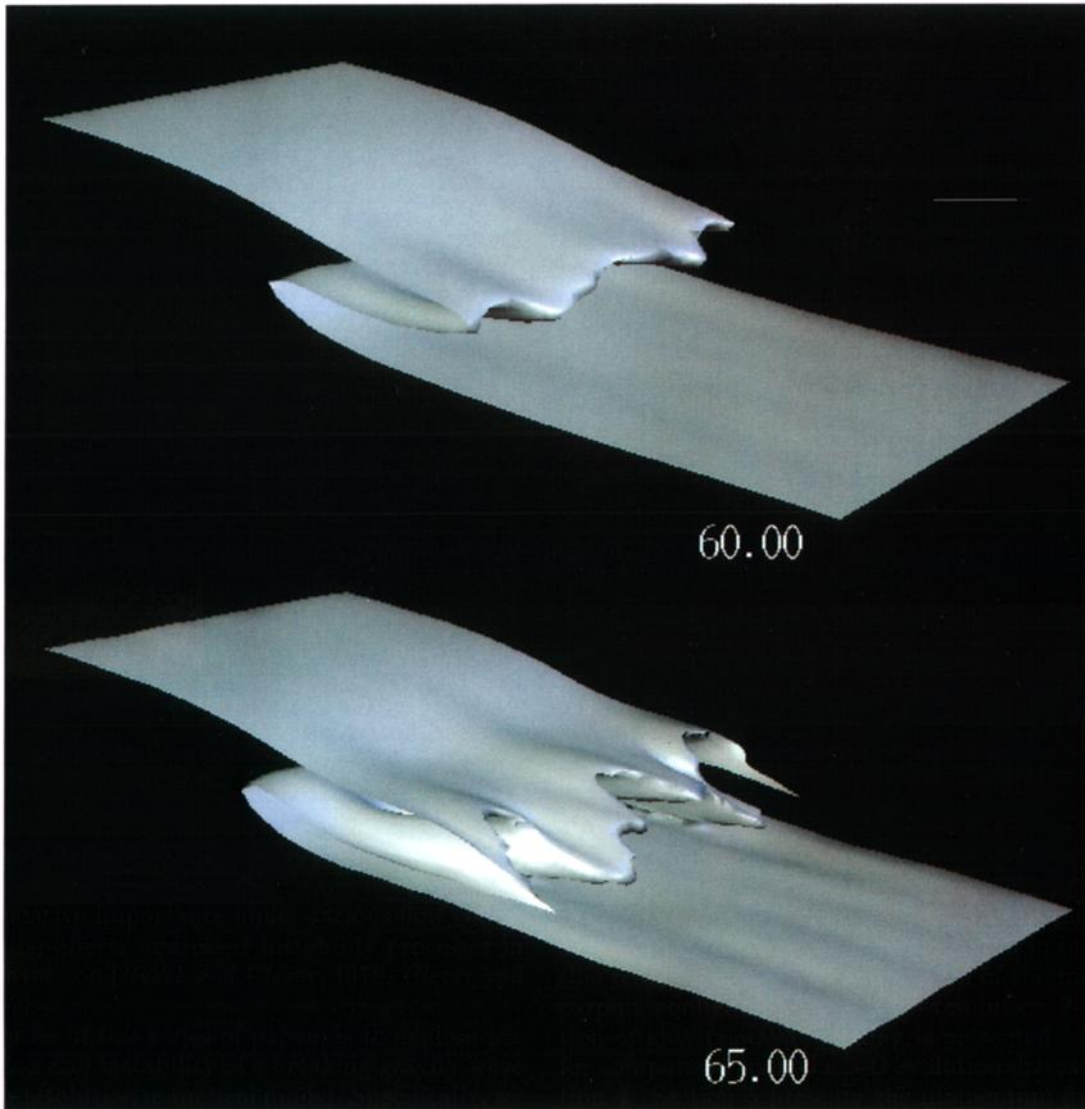


Plate 1. Potential temperature isosurface within the region of wave breaking for the three-dimensional simulation at $t = 60$ and 65 showing the emergence of instability structures. Wave propagation and positive x are toward the right.

Helmholtz (KH) instabilities and of their generation processes were provided in laboratory studies by *Browand and Troutt* [1980, 1985], *Breidenthal* [1981], *Jimenez* [1983], *Bernal and Roshko* [1986], and *Lasheras et al.* [1986]. Parallel theoretical and modeling studies by *Pierrehumbert and Widnall* [1982], *Nagata and Busse* [1983], *Klassen and Peltier* [1985], and *Metcalf et al.* [1987] examined the possible modes of instability and their relative importance under various flow conditions. Similar efforts addressed instability processes in sheared convection [*Busse and Clever*, 1979; *Clever and Busse*, 1992].

The purpose of this series of papers is to explore the 3-D evolution and instability of a breaking gravity wave with a high-resolution numerical model. Specifically, we will (1) contrast this evolution with that obtained with an equivalent 2-D model; (2) evaluate the effects of 3-D instability on wave propagation, amplitude growth, and energy and momentum fluxes; and (3) examine the scale selection, spectral character, and growth of the 3-D in-

stability. To enable the reader to appreciate the justification for such a study, we present in Plate 1 the potential temperature surface in the region of wave breaking at two times during transition to instability structures in the 3-D simulation. Our effort parallels in some respects a similar study by *Winters and D'Asaro* [1993] of the 3-D evolution of a gravity wave near a critical level in an ocean environment at lower resolution.

This paper is organized in the following manner. Our model formulation is presented in detail in section 2, as this represents the first application of the model in its current configuration. A high-resolution 2-D simulation of gravity wave breaking is presented in section 3 for comparison with the 3-D evolution discussed in section 4. Section 5 presents the momentum flux profiles and the resulting mean flow evolution observed in the 2-D and 3-D simulations and addresses the applicability of 2-D models to wave instability problems. Our comparison of wave field evolutions in 2-D and 3-D is summarized in section 6. The companion papers by *Fritts*

et al. [this issue] and *Isher et al.* [this issue] extend this analysis and focus, respectively, on the spectral evolution and structure of, and the energy and momentum transports by, the transverse ($k_y \neq 0$) 3-D instability and the subsequent transition to small-scale isotropic structure.

Model Formulation

Basic Equations

The model used for our studies of gravity wave breaking in two and three dimensions solves the equations expressing conservation of mass, momentum, and energy (the Euler equations) describing nonlinear dynamics in an inviscid, compressible, stratified fluid. Included in these equations, however, are terms representing an artificial diffusion to account for dissipation of energy at small scales in a manner permitting the physical description of processes occurring at larger scales of motion. These equations may be written in the form

$$\begin{aligned} \frac{\partial \rho}{\partial t} + \nabla \cdot (\rho \mathbf{v}) &= 0, \\ \rho \frac{d\mathbf{v}}{dt} &= -\nabla p + \rho \mathbf{g} + \mathbf{F} + \mathbf{P}, \\ \frac{dp}{dt} + \gamma p \nabla \cdot \mathbf{v} &= Q, \end{aligned} \tag{1}$$

where $\mathbf{v} = (u, v, w)$ is velocity, ρ is density, p is pressure, \mathbf{g} is the gravitational acceleration, and γ is the ratio of specific heats. The pressure and density are related to temperature through the equation of state, $p = \rho RT$, and we use the potential temperature, defined as $\theta = T(p_0/p)^{R/c_p}$ with p_0 a reference pressure, as an approximate tracer of fluid motions.

The additional terms in the momentum and adiabatic energy equations include a source term \mathbf{F} to excite gravity waves and artificial diffusion terms \mathbf{P} and Q to reduce the truncation errors caused by the nonlinear cascade of energy toward small spatial scales. The forms of these terms are described further below.

Spectral Representation and Spectral Diffusion

Equations (1) are solved in Cartesian coordinates (x, y, z) , using a spectral collocation method described by *Canuto et al.* [1988]. We use a Fourier/Chebyshev representation of the solution where trigonometric functions and Chebyshev polynomials describe the horizontal and vertical structure, respectively. As a result, our solutions are periodic in the horizontal directions and admit nonperiodic solutions and boundary conditions at the horizontal boundaries. We also nondimensionalize all variables with respect to the density scale height H , the sound speed c_s , with $c_s^2 = \gamma g H$, a timescale H/c_s , and a reference temperature T_0 , density ρ_0 , and pressure p_0 for this and subsequent discussions. With these choices the atmosphere is isothermal and the nondimensional Brunt-Väisälä frequency squared is $N^2 = (\gamma - 1)/\gamma^2$.

The solutions are approximated by expressions of the form

$$A(x, y, z, t) = \sum_{l=-N_x/2}^{N_x/2-1} \sum_{m=-N_y/2}^{N_y/2-1} \sum_{n=0}^{N_z} a_{lmn}(t) \cdot \exp\{2\pi i(lx + my)\} T_n(z), \tag{2}$$

where the a_{lmn} are complex coefficients and

$$T_n(z) = \cos(n \arccos(z)) \tag{3}$$

is the Chebyshev polynomial of order n . The domain of definition of the basis functions is $0 \leq x < 2\pi$, $0 \leq y < 2\pi$, and $-1 \leq z \leq 1$. The computational domains are defined by (x_0, y_0, z_0) , the nondimensional domain sizes appropriate to each of two domains (see below). This choice of basis functions leads to a set of collocation points given by

$$(x_l, y_m, z_n) = (2\pi l/N_x, 2\pi m/N_y, \cos(2\pi n/N_z)), \tag{4}$$

with $0 \leq l \leq N_x - 1$, $0 \leq m \leq N_y - 1$, and $0 \leq n \leq N_z$. Spatial derivatives in the governing equations are then computed using fast Fourier transforms and Chebyshev recursion relations in a manner following *Canuto et al.* [1988], permitting a high degree of utilization of present vector/parallel computers.

The diffusion terms \mathbf{P} and Q are represented as spectral diffusion in our model formulation. This approach was suggested by *Tadmor* [1989], who applied the method to one-dimensional shock waves, and adopted for a Fourier/Chebyshev method for the present problem by *Andreassen et al.* [1993]. These diffusion terms are

$$P_i = \sum_{j=1}^3 \varphi_j(z) \frac{\partial}{\partial x_j} \left(\mu_j \star \frac{\partial v_i}{\partial x_j} \right), \quad i = 1, 2, 3 \tag{5}$$

$$Q = (\gamma - 1) \sum_{j=1}^3 \varphi_j(z) \frac{\partial}{\partial x_j} \left(\kappa_j \star \frac{\partial T}{\partial x_j} \right), \tag{6}$$

where the stars denote multiplication in spectral space, $\mathbf{x} = (x, y, z)$ is the nondimensional position vector, $\mathbf{k} = (k_x, k_y, k_z)$ is the nondimensional wavenumber vector, and T is nondimensional temperature.

The spectral viscosity coefficient μ_i is written in the form

$$\mu_i = (\mu_0/N_i) \mu_i(k_i), \tag{7}$$

where N_i is the number of collocation points in direction x_i , with the kinematic spectral viscosity varying inversely with density as

$$\nu_i = \mu_i/\rho. \tag{8}$$

The expression for thermal diffusivity is likewise given by

$$\kappa_i = (\kappa_0/N_i) \kappa_i(k_i). \tag{9}$$

Finally, the functional forms of the Chebyshev weight function φ and of the component spectral diffusion coefficients $\nu_i(k_i)$ and $\kappa_i(k_i)$ are

$$\varphi_i(z) = \begin{cases} 1, & i = 1, 2, \\ \sqrt{1 - z^2}, & i = 3 \end{cases} \tag{10}$$

$$\nu_i(k_i), \kappa_i(k_i) \begin{cases} 0, & k_i < \alpha\sqrt{N_i}, \\ 1 - \alpha^2 N_i/k_i^2, & k_i \geq \alpha\sqrt{N_i}, \end{cases} \quad (11)$$

where $\alpha \approx 1.5$ is an empirical constant and N_i is the number of collocation points in direction i . This formulation of the diffusion has the advantages that it damps small scales in a manner similar to eddy diffusion, it leaves larger scales unaffected by dissipation, and the method can be proven to converge for several problems involving conservation laws as the threshold wavenumbers increase and the diffusion coefficients decrease with increasing N_i as in equation (7) [Maday and Tadmor, 1989; Chen et al., 1992; Maday et al., 1993].

The dissipation terms in equations (1), given formally by equations (5) and (6), may be expressed at high wavenumbers as $\nabla(\nu \cdot \nabla \mathbf{v})$ in the momentum equation (after dividing by density) and $\nabla(\kappa \cdot \nabla T)$ in the energy equation, where ν is the kinematic viscosity coefficient, κ is the thermal diffusion coefficient, and the ratio of these is the Prandtl number, $Pr = \nu/\kappa$, which is ≈ 0.71 for air [Landau and Lifshitz, 1959]. These dissipation terms were tuned in our code to provide physical spectral energy variations at large wavenumbers in order to avoid energy accumulation near the maximum wavenumbers in the region of wave instability at intermediate levels of the upper domain. For the simulation results presented here, these coefficients were taken to be $\nu \approx 0.03$ and $\kappa \approx 0.05$ (nondimensionally) at the center of the upper domain, with values at the lower boundary of the lower domain of $\nu_0 = 0.0003$ and $\kappa_0 = 0.0005$.

Time Integration

Solutions were advanced in time using an explicit second-order Runge-Kutta method with variable time steps to provide efficient computation for large scales of motion and to insure numerical stability as energy cascaded to smaller spatial scales. Variable time steps also served as a tool to monitor the calculations and aid in tuning the spectral diffusion parameters discussed above.

The required accuracy in our simulations was moderate in the ODE sense and the function evaluations were computationally expensive ($\sim 80 - 90\%$ of total computing time) and required large memory, suggesting that a low-order method should be used. As a result, the widely used Runge-Kutta codes RK45 and DOPRI5 requiring six and seven function evaluations per step were judged to be too expensive for our applications. Our choice instead was a second-order scheme with third-order error estimation, RK2(3) [Andreassen et al., 1993]. Because the solutions varied strongly with height, it was also necessary to introduce a set of weighting functions to provide comparable sensitivity of the error estimator at all heights and for each physical variable. This yielded an increase in the time steps and a reduction in computing times by an order of magnitude.

Domain Decomposition, Matching and Boundary Conditions

Our spectral collocation code was designed to provide efficient simulations of compressible dynamics in

two and three spatial dimensions. As such, it was constructed using two model domains in the vertical because Chebyshev computational requirements vary as $\sim N_z^2$ in each domain. Thus multiple domains stacked on top of each other can be more efficient than a single large domain with the same number of Chebyshev collocation points [Wasberg, 1992]. A further efficiency was achieved by allowing different N_i in the two domains to provide resolution where it was needed and to focus computational resources on the most relevant physics. In this particular experiment the lower and upper domains were scaled to nondimensional depths of $z_{1,0} = 4$ and $z_{2,0} = 1.5$, with the first subscripts referring to the lower and upper domains, respectively, and each domain had horizontal dimensions $x_0 = 4$ and $y_0 = 2$. The horizontal components of the solution were required to be periodic given our choice of Fourier decomposition in x and y . Matching conditions at the interface between domains were specified by using the upwind characteristic values at the interface. This insured continuity of the field variables between domains.

Finally, open boundary conditions were imposed at the lower boundary of the lower domain and the upper boundary of the upper domain to insure propagation of wave energy originating within the model domains outward with minimum influences of wave reflection on the interior solution. These boundary and interface conditions were formulated using pseudo-one-dimensional characteristics to describe propagation near the boundary/interface, as described by Wasberg and Andreassen [1990] and Andreassen et al. [1992].

It is convenient to write equations (1) in vector form,

$$\mathbf{U}_t + \mathcal{A}\mathbf{U}_x + \mathcal{B}\mathbf{U}_y + \mathcal{C}\mathbf{U}_z + \mathbf{b} = D^2\mathbf{U}, \quad (12)$$

where subscripts denote partial derivatives,

$$\mathbf{U} = \begin{bmatrix} \rho \\ u \\ v \\ w \\ p \end{bmatrix}, \quad \mathcal{A} = \begin{bmatrix} u & \rho & 0 & 0 & 0 \\ 0 & u & 0 & 0 & 1/\rho \\ 0 & 0 & u & 0 & 0 \\ 0 & 0 & 0 & u & 0 \\ 0 & \gamma p & 0 & 0 & u \end{bmatrix},$$

$$\mathcal{B} = \begin{bmatrix} v & 0 & \rho & 0 & 0 \\ 0 & v & 0 & 0 & 0 \\ 0 & 0 & v & 0 & 1/\rho \\ 0 & 0 & 0 & v & 0 \\ 0 & 0 & \gamma p & 0 & v \end{bmatrix}, \quad (13)$$

$$\mathcal{C} = \begin{bmatrix} w & 0 & 0 & \rho & 0 \\ 0 & w & 0 & 0 & 0 \\ 0 & 0 & w & 0 & 0 \\ 0 & 0 & 0 & w & 1/\rho \\ 0 & 0 & 0 & \gamma p & w \end{bmatrix}, \quad \mathbf{b} = \begin{bmatrix} 0 \\ 0 \\ 0 \\ g \\ 0 \end{bmatrix},$$

and the term $D^2\mathbf{U}$ is the dissipation term.

To treat the horizontal boundaries, the matrixes \mathcal{A} and \mathcal{B} are ignored and the vertical contribution of \mathcal{D} vanishes at the horizontal boundaries because of the Chebyshev weight functions (see equation (10)). The elements of \mathcal{C} are assumed to be slowly varying and denoted with hats such that

$$\mathbf{U}_t + \hat{C}\mathbf{U}_z = -\mathbf{b}. \tag{14}$$

The eigenvalues and corresponding left eigenvectors of \hat{C} are

$$\begin{aligned} \lambda_1 &= \hat{w} - \hat{c}_s, & \mathbf{l}_1 &= \{0, 0, 0, -\hat{\rho}\hat{c}_s, 1\}, \\ \lambda_2 &= \hat{w}, & \mathbf{l}_2 &= \{0, 1, 0, 0, 0\}, \\ \lambda_3 &= \hat{w}, & \mathbf{l}_3 &= \{0, 0, 1, 0, 0\}, \\ \lambda_4 &= \hat{w}, & \mathbf{l}_4 &= \{1, 0, 0, 0, -1/\hat{c}_s^2\}, \\ \lambda_5 &= \hat{w} + \hat{c}_s, & \mathbf{l}_5 &= \{0, 0, 0, \hat{\rho}\hat{c}_s, 1\}, \end{aligned} \tag{15}$$

where \hat{c}_s is the sound speed. The characteristic variables are defined as $\psi_i = \beta_i(\mathbf{l}_i \cdot \mathbf{U})$ with $i = 1, \dots, 5$. Then choosing $\beta_i = 1$, we obtain

$$\psi = \begin{bmatrix} -\hat{\rho}\hat{c}_s w + p, \\ u, \\ v, \\ \rho - p/\hat{c}_s^2, \\ \hat{\rho}\hat{c}_s w + p. \end{bmatrix} \tag{16}$$

$$\mathbf{U} = \begin{bmatrix} \psi_4 + (\psi_1 + \psi_5)/2\hat{c}_s^2 \\ \psi_2 \\ \psi_3 \\ (\psi_5 - \psi_1)/2\hat{\rho}\hat{c}_s \\ (\psi_1 + \psi_5)/2 \end{bmatrix}. \tag{17}$$

To construct conditions at the upper and lower boundaries, we note that ‘‘information’’ carried along the first and last characteristics is propagated with the sound speed in both directions relative to an observer moving with the fluid, while the intermediate characteristics carry ‘‘information’’ with the velocity of the fluid. As long as the velocity is subsonic, there will be one inflow and one outflow fast characteristic, while the direction of the slow characteristics might change, depending on the solution. Whether inflow or outflow conditions apply for a specified location is determined at the previous time step. The variables corresponding to the slow inflow characteristics are related to the values near the boundary using an extrapolation procedure based on the interior neighboring values at the previous time step. The variables corresponding to the fast incoming characteristic are equated to the values obtained assuming hydrostatic equilibrium. This gives smooth and stable results. The conditions at the interface between domains are formulated by using outflow information from each domain to calculate the five characteristic variables and solve the system obtained for the physical variables at the new time step.

Model Environment and Gravity Wave Forcing

Initially, the medium was assumed to be in hydrostatic equilibrium with constant nondimensional temperature $T = 1$ and a horizontal mean motion given by

$$U_0(z) = \begin{cases} 0, & 0 \leq z \leq 4, \\ 0.2(1 + \cos\{(3 - z/2)\pi\}), & 4 \leq z \leq 5.5. \end{cases} \tag{18}$$

The role of this shear flow was to confine the dominant wave activity within the upper model domain and avoid

small-scale structures near domain boundaries. This function was selected such that the velocity $U_0(z)$ at $z = 5$ was equal to the horizontal phase speed of the forced wave, yielding an initial critical layer at that height.

A gravity wave was forced in the lower domain by a vertical body force of the form

$$f(x, z, t) = f_0 \xi(t) e^{-(z-\delta)^2/\sigma^2} \sin\{\omega t - k_0 x\} \tag{19}$$

$$\xi(t) = \begin{cases} \sqrt{t/10}, & 0 \leq t \leq 10, \\ 1, & 10 < t \leq 50, \\ \sqrt{(t-50)/10}, & 50 < t \leq 60, \\ 0, & 60 < t, \end{cases} \tag{20}$$

where $f_0 = 0.02$ is the forcing amplitude, $\delta = 3$ is the height of maximum force, and $\sigma = 0.5$ expresses the width of the forcing. The horizontal wavenumber of the forcing was $|k_0| = 2\pi/x_0 = \pi/2$ and corresponds to a wavelength equal to the domain length. The frequency of the forcing was chosen to be $\omega = \pi/10$, which is slightly below the Brunt-Väisälä frequency and corresponds to a horizontal phase speed of $c = 0.2$ and the initial mean horizontal velocity at $z = 5$.

This forcing excited a gravity wave which increased smoothly in amplitude with time and decreasing density and which yielded rapid vertical propagation and instability at upper levels. This resulted in initial convective instability in the upper domain near $t \simeq 37$ and $z \simeq 4.75$. At this time and location the intrinsic phase speed and period of the wave motion were $\sim 20 \text{ ms}^{-1}$ and $\sim 20 \text{ min}$ and are representative of those gravity wave motions accounting for the dominant energy and momentum fluxes in the mesosphere and lower thermosphere.

Interpolation and Initiation of Three-Dimensional Structure

Our major objective in this series of papers is the description of the transition from 2-D to 3-D flows as a consequence of gravity wave breaking. Given this, the 3-D simulations were initiated from 2-D simulations at lower resolution at a time shortly before the occurrence of convective instability. With convective instability first occurring near $t = 37$, we converted to higher spatial resolution in x and z , added a transverse (y or spanwise) dimension, and inserted a broad, weak 3-D noise spectrum at $t = 35$ to allow the subsequent flow instability to evolve in a physical manner. Without noise insertion the solution would have remained purely 2-D indefinitely.

Interpolation to a finer mesh was accomplished by simply increasing the number of spectral components N_i in x and z with zero initial amplitude. A third dimension was added in a similar manner by associating all 2-D structures with $k_y = 0$ and allowing for the subsequent evolution of and interactions among nonzero k_y initiated by the insertion of a 3-D noise field.

The 3-D noise spectrum was introduced into the density field to trigger those instabilities that were favored

Potential Temperature and Velocity Fields

The 2-D evolution is displayed with contours of potential temperature and perturbation velocity vectors in a reference frame moving with the gravity wave horizontal phase speed at intervals of $\Delta t = 5$ from $t = 55$ to 90 in Figures 1 and 2. These reveal a 2-D breaking structure in qualitative agreement with the results of *Winters and D'Asaro [1989]* and *Walterscheid and Schubert [1990]*, with approximately isotropic rolling structures initiated within regions of convective instability. These rolls appear to result from the fluid motion exceeding the horizontal wave phase speed near the wave crest and contribute to the extraction of energy from the primary gravity wave. Nevertheless, the linear stability analysis by *Winters and Riley [1992]* suggests that these structures may be a manifestation of dynamical instability. This interpretation is supported by very large values of the local velocity shear (see the discussion of Figure 9 in section below) near the time at which these structures

begin to form ($t \sim 70$), which suggest local values of the Richardson number based on the large-scale wave and mean motions of $Ri \sim 0.1$ or less. The billow structures that result have initial orientations with generally negative correlations of u' and w' , where primes denote eddy fields and positive fluctuations are in the direction of horizontal wave propagation and upward, consistent with a downward transport of positive (x) momentum needed to stabilize the local shear flow (see Figures 1 and 2).

As the evolution proceeds, there is evidence of initial pairing of adjacent vortex structures and an apparent smooth, continuing transfer of wave energy to smaller scales. In particular, the billow structures in the bottom left-hand portion of the panels displayed in Figures 1 and 2 appear to increase in amplitude until $t \sim 85$, at which time their vertical extent exceeds the vertical wavelength of the incident gravity wave. Thereafter, these billows begin to decay as additional eddy structures appear and energy is dissipated at smaller scales

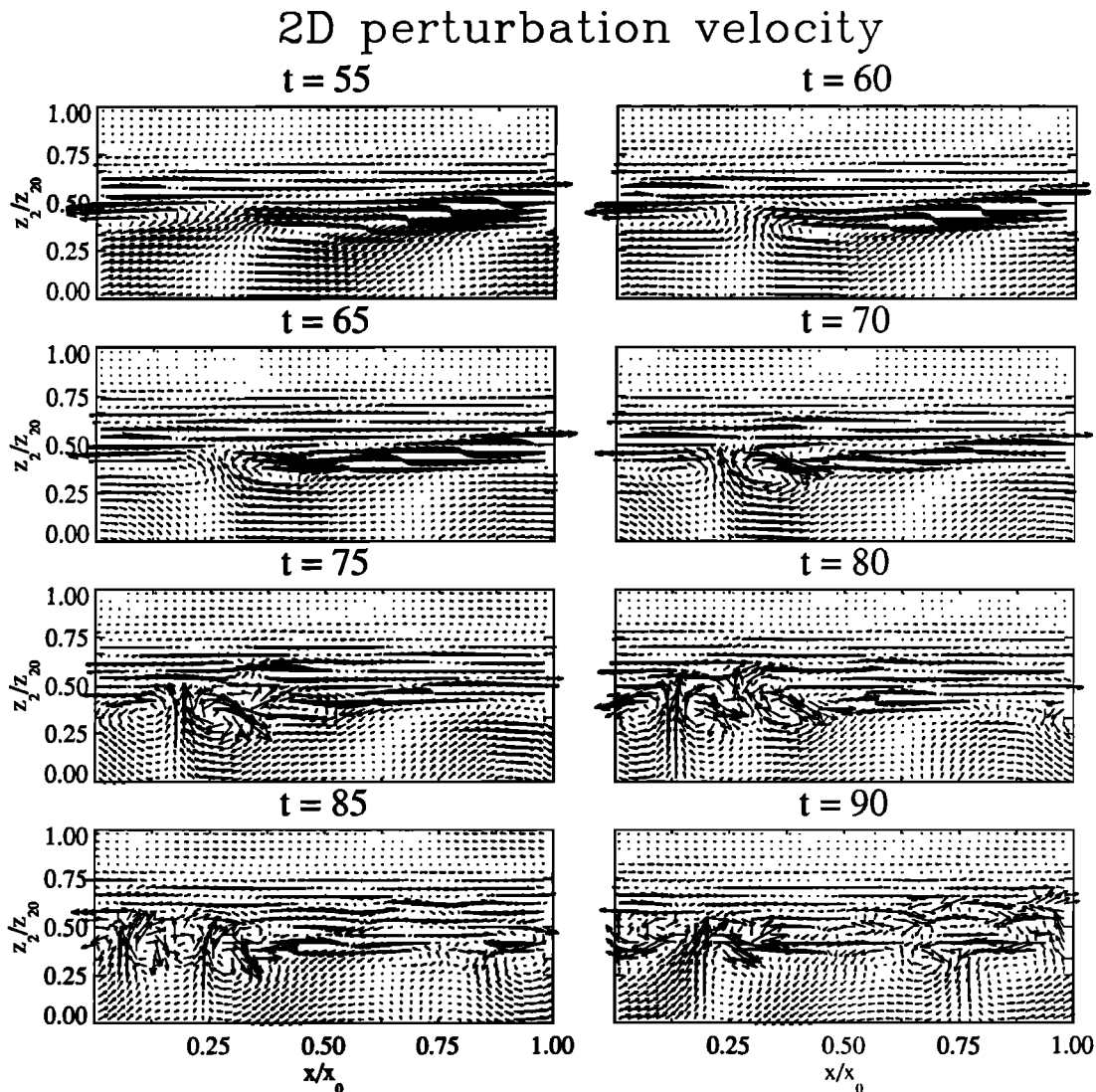


Figure 2. Perturbation velocity vectors for the simulation and times shown in Figure 1.

throughout the wave field. The small-scale flow features are accentuated with the perturbation velocity vectors in Figure 2 which show more clearly the departures from the incident wave structure and the sites of eddy kinetic energy enhancements.

The effects of this nonlinear 2-D evolution on the amplitude of the primary wave are seen in the potential temperature fields in Figure 1. These reveal a tendency for the wave motion to be saturated by the nonlinear transfer of energy to smaller scales but with persistent regions of convective instability and a significant degree of supersaturation due to the gradual rate of this transfer. Another measure of the degree of supersaturation of the incident wave motion is provided by comparing horizontal perturbation velocities with the intrinsic horizontal phase speeds at those heights. The phase speeds computed from the vertical wavelength of the incident wave motion (but not shown) reveal perturbation velocities exceeding their nominal saturated amplitudes by ~ 30 to 50% throughout much of the region of wave instability.

Two-Dimensional Kinetic Energy at Small Scales

The evolution and energetics of small-scale structures in the 2-D simulation are characterized using the spectral distribution of kinetic energy in x and the kinetic energy for various k_x averaged over the layer $0.2 \leq z_2/z_{2,0} \leq 0.6$ as functions of time. Energy-content spectra are shown in Figure 3 to illustrate the dominant scales of the wave and eddy structures at the level of wave breaking. The averaged kinetic energy shown in Figure 4 better illustrates the global exchange of energy among the various components of the motion field.

Referring to Figure 3, we note that instability is preceded by a nonlinear transfer of energy from the forced gravity wave to its harmonics at smaller horizontal scales, primarily $|k_x| = \pi$ and $3\pi/2$ (wavenumbers 2 and 3 relative to the horizontal domain). Once instability has occurred (after $t \sim 60$), however, the dominant

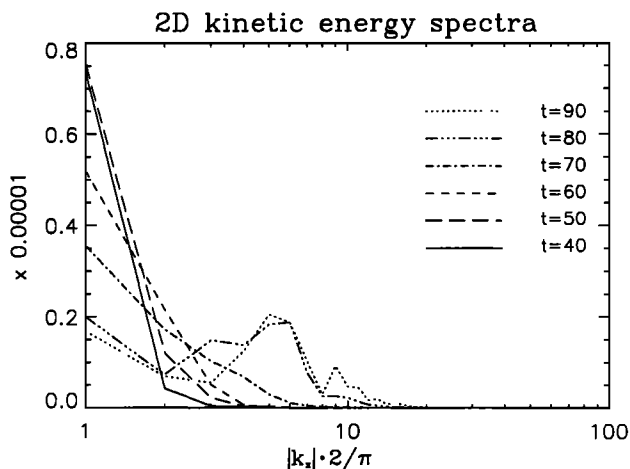


Figure 3. Energy-content spectra of kinetic energy, $E_k(k_x)$, for the two-dimensional gravity wave simulation at $t = 40, 50, 60, 70, 80,$ and 90 .

response is at larger wavenumbers, with maximum amplitudes at $|k_x| \sim 2\pi$ to 3π , corresponding to the small-scale structures seen in Figures 1 and 2. Wavenumbers $|k_x| = \pi$ and $3\pi/2$ are found to have phase structures in approximate agreement with the incident wave in the region of primary wave breaking, with evanescent structures at higher and lower levels due to outward propagation and increasing intrinsic phase speeds. Higher harmonics are more nearly confined to the breaking region and do not exhibit a clear phase structure with z .

The instability growth and its influences on the incident gravity wave are illustrated more clearly in Figure 4. Here we see that the incident wave ceases growth and begins a gradual decay at $t \sim 40$, due to the decrease of wave forcing in the lower domain beginning at $t = 50$, the evolution toward smaller vertical scales within the wave field, and the associated reduction of energy transports into the region of wave breaking. Harmonics of the incident wave with clear phase structure achieve their maximum amplitudes somewhat later, with energy at smaller scales growing rapidly during this interval in response to wave field instability and achieving a maximum at $t \sim 85$. It will be seen below, however, that the gravity wave amplitude obtained in this 2-D simulation is substantially larger than that occurring when 3-D instabilities are permitted to evolve within the wave field.

Three-Dimensional Gravity Wave Breaking

To contrast gravity wave breaking in two and three dimensions, we present here results of a simulation performed with the same maximum resolution as above, but with a third dimension included with equal transverse resolution. This simulation was performed with

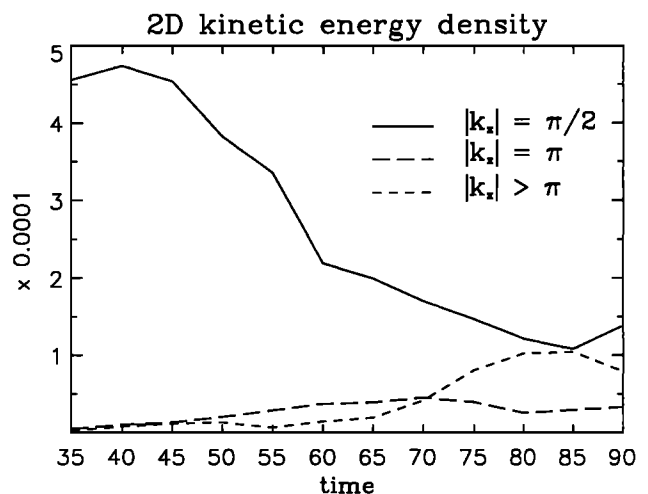


Figure 4. Kinetic energies in the upper domain averaged over $0.2 < z_2/z_{2,0} < 0.6$ for the two-dimensional gravity wave simulation from $t = 35$ to 90 . Solid, dashed, and dotted curves show the $|k_x| = \pi/2, \pi,$ and $> \pi$ contributions, respectively.

Fourier-Fourier-Chebyshev representation in (x, y, z) , with $96 \times 48 \times 49$ components in the upper domain, $64 \times 32 \times 33$ components in the lower domain, x_0 and $z_{2,0}$ as above, and $y_0 = 2$ in each domain. This yields isotropic resolution in the domain interiors and an ability to follow the evolution of small-scale flow features toward isotropic motions in response to wave instability and the resulting energy cascade toward small scales. As in the 2-D simulation discussed above, the 3-D simulation presented here was extended to $t = 90$ to describe both the rapid initial instability evolution and its subsequent breakdown and transition to smaller-scale, isotropic motions. Results are again displayed only in the upper domain as this was where the gravity wave achieved an unstable amplitude.

Three-Dimensional $k_y = 0$ Potential Temperature and Velocity Fields

To assess the effects of the 3-D transverse ($k_y \neq 0$) instability on the incident wave amplitude, we show in Figures 5 and 6 the potential temperature and pertur-

bation velocity fields obtained for the $k_y = 0$ components of the motion field at times corresponding to those fields in Figures 1 and 2. These reveal striking differences between the 2-D and the 3-D $k_y = 0$ evolutions and the amplitude limits imposed on the incident gravity wave by small-scale instability structures in each case. Whereas the 2-D evolution exhibits substantial, persistent overturning of the wave field and sustained and energetic activity at smaller scales, the 3-D evolution undergoes a rapid collapse of the initially large region of convective instability (due to the small initial noise amplitude) and is constrained at later times by the more vigorous vortex structures described in detail in the companion paper by *Fritts et al.* [this issue].

Differences between the two evolutions begin to appear as early as $t = 65$ in the 2-D and 3-D $k_y = 0$ fields shown. In each case, an isolated region of high potential temperature is observed to form in response to the initial wave overturning and to persist until $t \sim 75$. But while this feature is entrained by the vigorous 2-D rolling structures in the 2-D simulation, no correspond-

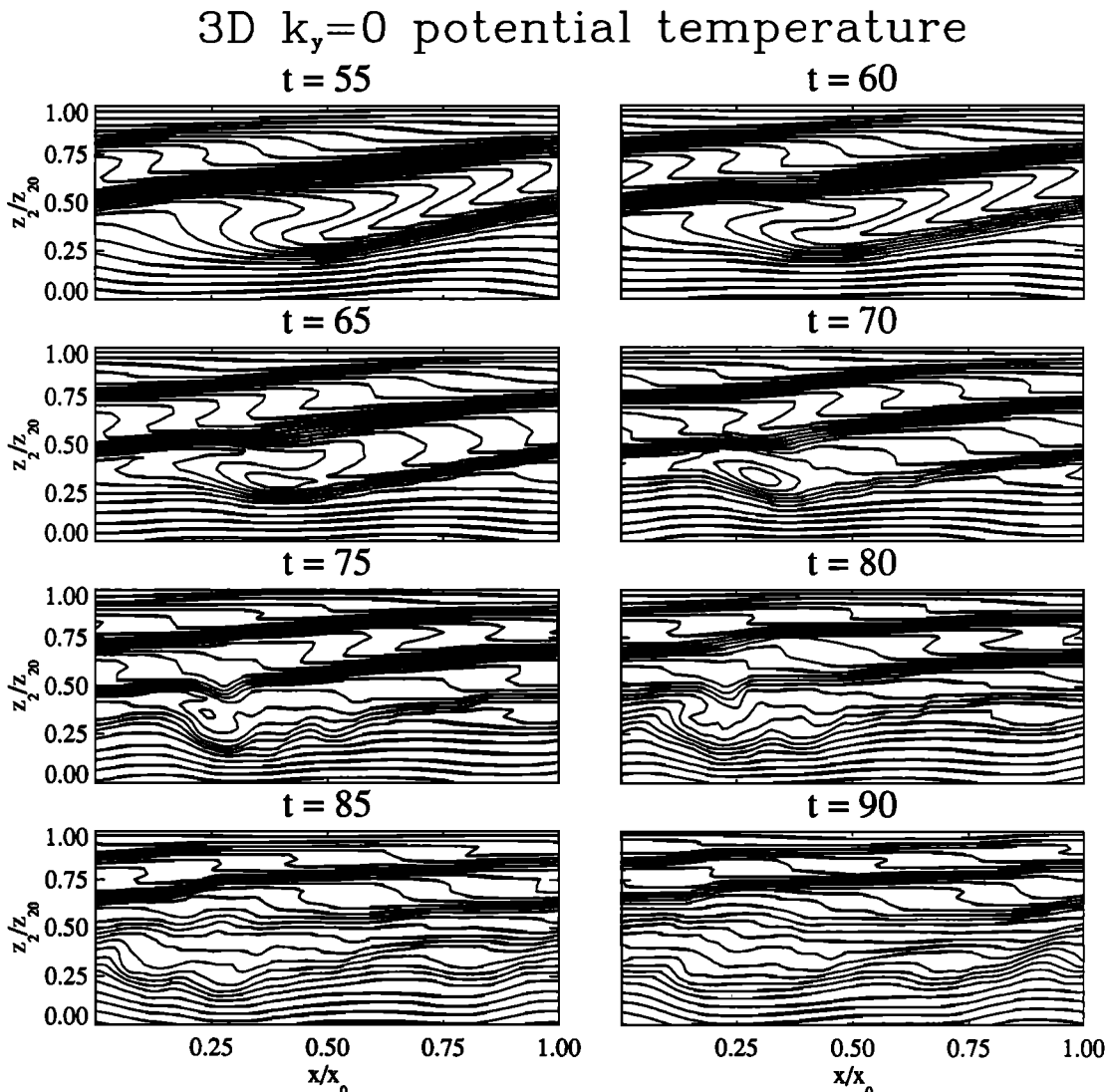


Figure 5. Contours of potential temperature for the $k_y = 0$ components of the three-dimensional gravity wave simulation at the times displayed in Figure 1.

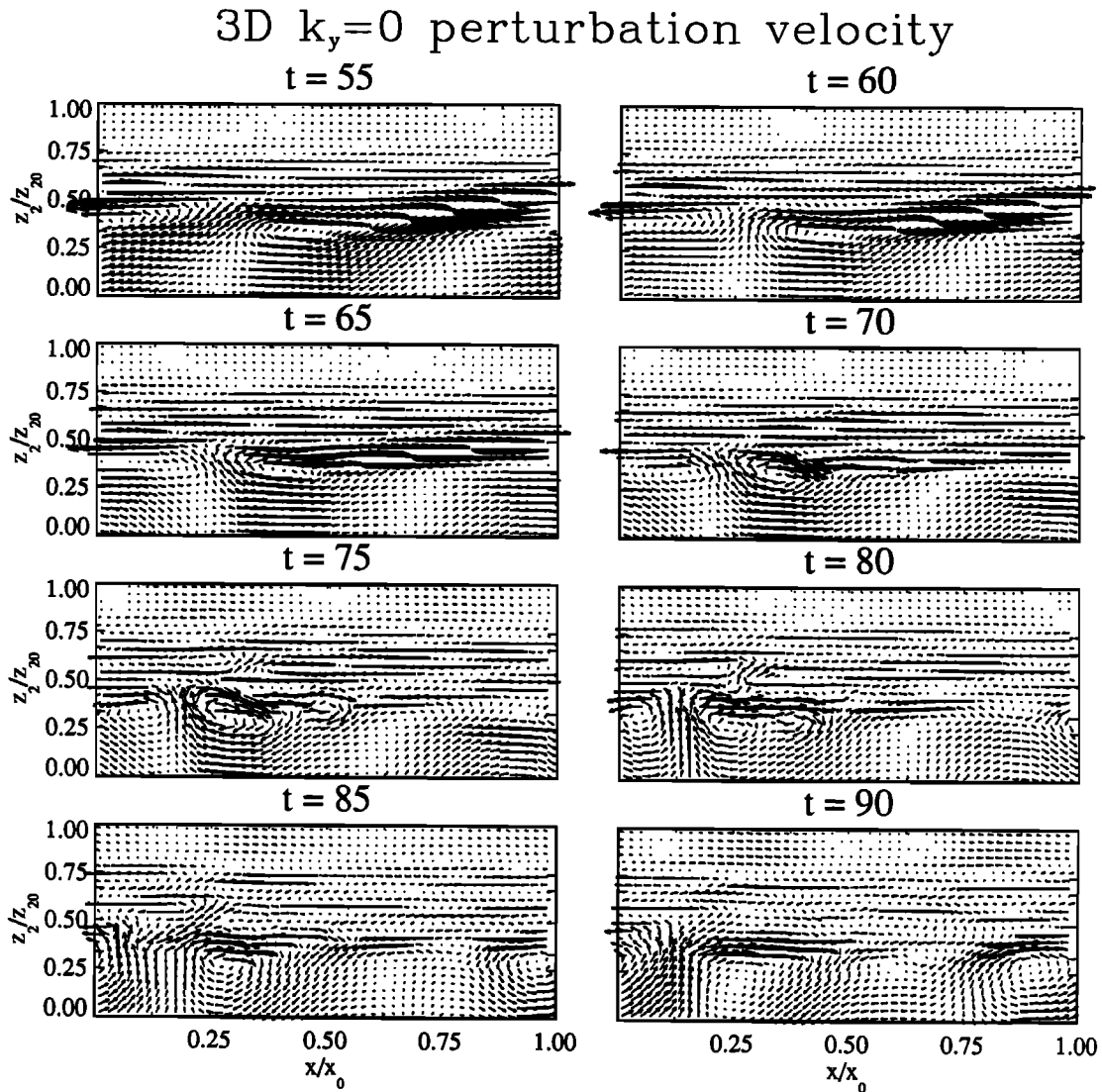


Figure 6. Perturbation velocity vectors for the $k_y = 0$ components of the three-dimensional gravity wave simulation at the times displayed in Figure 2.

ing evolution or energetic 2-D motions are seen to occur in the 3-D simulation at later times. The 3-D wave collapse and energy transfer from the incident wave to the instability structures has no signature in the $k_y = 0$ motion field such as seen in the 2-D evolution shown in Figures 1 and 2. Instead, the dominant energy transfers and fluxes in the 3-D evolution are due to small-scale structures that are inherently three dimensional, with motions and vorticity in all three directions. These structures also clearly are much more effective at limiting the incident wave amplitude as early in the evolution as $t \sim 65$, where the degree of overturning in the 3-D $k_y = 0$ potential temperature field is already substantially less than in the corresponding 2-D simulation. These departures accelerate with time, resulting in nearly adiabatic regions (as opposed to extended superadiabatic regions in the 2-D simulation) and much smaller wave velocities at heights of initial wave instability. At greater heights the 3-D $k_y = 0$ wave amplitudes are constrained to values smaller than in the 2-D sim-

ulation by the more rapid evolution of 3-D instability structures at smaller scales.

The perturbation velocity fields likewise reveal large differences between the 2-D and the 3-D $k_y = 0$ evolutions (Figures 2 and 6). Until $t = 70$, the two fields are almost identical. Clear differences are apparent as early as $t = 75$, however, where the 3-D $k_y = 0$ fields exhibit similar structures but with substantially smaller amplitudes. At later times the strong two-cell structure seen in the 2-D evolution is replaced by a weaker, single cell and eddy structures throughout the domain are strongly suppressed in the 3-D $k_y = 0$ evolution. The relative energetics of the two simulations are addressed in more detail below.

Given the comparisons presented above, it appears that 2-D simulations are largely unable to describe either the instability processes contributing to wave saturation or the implications of wave breaking for spectral evolution and transports of energy, momentum, heat, and constituents for gravity waves at higher intrinsic

frequencies. However, our results also suggest that 2-D simulations with an appropriate convective adjustment scheme may capture some of the qualitative effects of 3-D instability on wave amplitudes and transports.

Three-Dimensional Kinetic Energy at Small Scales

The energetics of small-scale structures in the 3-D simulation are assessed as in the 2-D simulation discussed above but with the kinetic energy computed separately for motions with $k_y = 0$ and $k_y \neq 0$ to compare the energy transfers in the two simulations. Prior to $t = 60$, the 2-D and 3-D simulations are virtually identical, with a nonlinear excitation of harmonics of the incident wave (at $k_y = 0$) and a gradual decay of incident wave energy due to the evolution of the mean wind profile. Thereafter, however, the evolutions of the 2-D and 3-D simulations diverge in important ways. Whereas the 2-D simulation displays strong growth of the KH structures at smaller scales ($|k_x| > \pi$), the 3-D simulation exhibits much weaker growth of the higher harmonics at $k_y = 0$ and much more rapid growth (approximately twice the growth rate of the 2-D motions at large $|k_x|$) of the kinetic energy of structures with $k_y \neq 0$ (see Figure 7). This eddy kinetic energy growth in the 3-D simulation is associated with vortex structures that distort the isosurfaces of potential temperature in Plate 1 and which are discussed further by *Fritts et al.* [this issue]. These structures are a consequence of the primary mode of convective instability of the primary wave motion when the evolution is not artificially constrained to two dimensions. The $k_y \neq 0$ eddy structures grow approximately exponentially until $t \sim 70$ and achieve a maximum at $t \sim 75$, at which time the instability is fully developed and strongly influencing the

incident wave structure. Thereafter, the primary wave is constrained to amplitudes very much smaller than permitted in the 2-D simulation because of the much more efficient energy extraction by the transverse, 3-D instability.

Comparison of Momentum Fluxes and Mean Flow Evolutions

We now consider the relative transports of momentum by the incident wave and the small-scale structures occurring in the 2-D and 3-D simulations in order to contrast their influences on the mean velocity field. Thus we present profiles of the vertical flux of horizontal momentum (per unit mass), $\overline{u'w'}$, for the incident gravity wave, its harmonics at $|k_x| > 1$ and $k_y = 0$, and the instability structures at $k_y \neq 0$ from $t = 40$ to 90 for the 2-D and 3-D simulations in Figure 8. The net effects of these transports for the mean velocity profile in each case are compared in Figure 9.

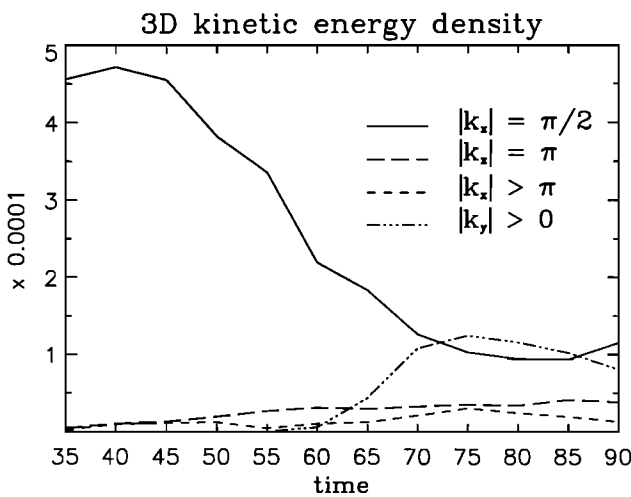


Figure 7. Kinetic energies in the upper domain averaged over $0.2 < z_2/z_{2,0} < 0.6$ for the three-dimensional gravity wave simulation from $t = 35$ to 90. Solid, dashed, and dotted curves show the $|k_x| = \pi/2, \pi,$ and $> \pi$ contributions, respectively, for $k_y = 0$. A dashed-dotted curve shows the $k_y \neq 0$ contribution representing the three-dimensional instability structures.

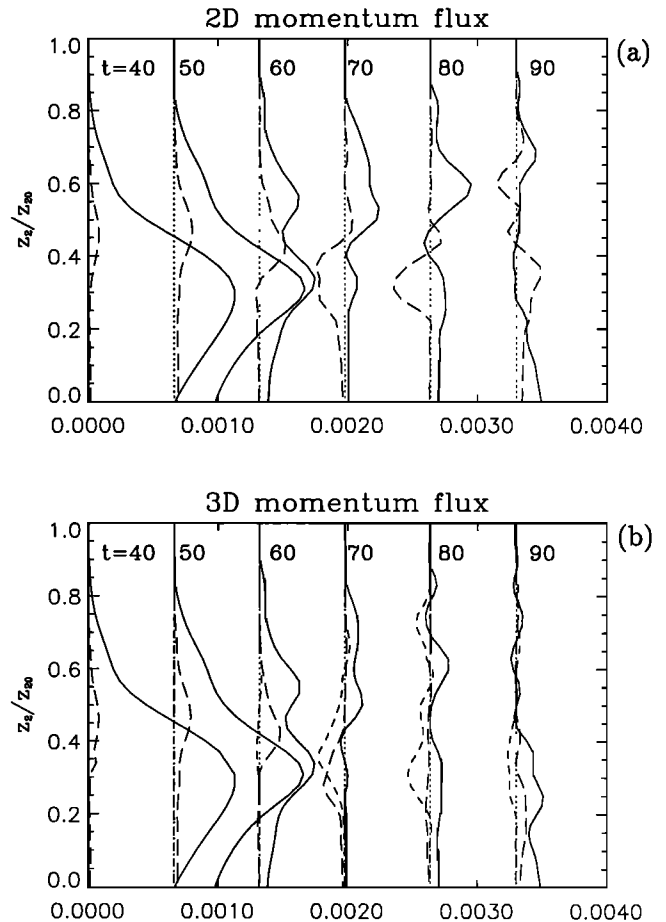


Figure 8. Profiles of the vertical flux of horizontal (zonal) momentum for the incident gravity wave (solid), its harmonics with $|k_x| > \pi/2$ and $k_y = 0$ (long-dashed), and the instability structures with $k_y \neq 0$ (short-dashed) obtained in the (a) two-dimensional and (b) three-dimensional gravity wave simulations at $t = 40, 50, 60, 70, 80,$ and 90. Successive profiles are displaced by 0.0007.

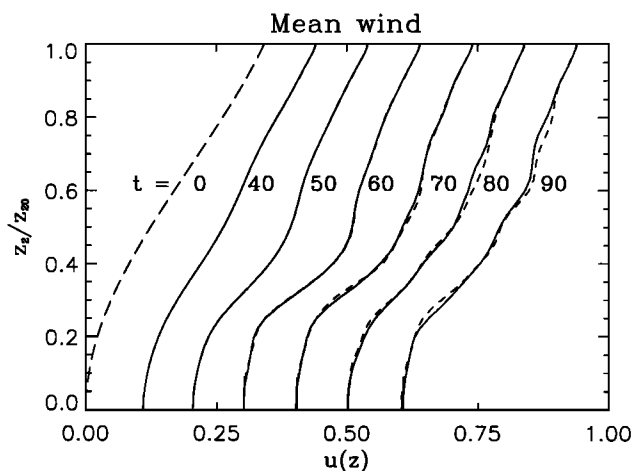


Figure 9. Mean velocity profiles for the two-dimensional (dashed) and three-dimensional (solid) gravity wave simulations at the times shown in Figure 8. Successive profiles are displaced by 0.1 and the initial profile is shown as a dashed curve at the left.

Wave and Eddy Momentum Fluxes

The 2-D and 3-D simulations exhibit almost identical wave fluxes of momentum prior to the attainment of energetic instability structures and their associated limits on the incident wave amplitude. Because the instability structures evolve much more rapidly in the 3-D simulation, however, the incident wave fluxes of momentum in this case are strongly suppressed by $t \sim 70$ and much reduced thereafter. This evolution proceeds more slowly in the 2-D simulation, with larger fluxes persisting until later times.

Harmonics of the incident wave are excited in both simulations as the incident wave motion achieves large amplitude. In each case, these contribute positive fluxes at intermediate levels and early times ($t \sim 60$), suggesting wave structures with common phase slopes and directions of propagation with the incident wave. Somewhat later, however, both 2-D ($k_y = 0$) and 3-D ($k_y \neq 0$) eddy structures contribute fluxes which are initially positive above and negative below the region of primary wave breaking, due to the negative and positive wave and mean shears at these locations (see Figures 2 and 6). The eddy fluxes transition to large negative fluxes at lower levels and later times ($t \sim 70$ to 80), due to the excitation of KH instabilities (the rolling structures seen in Figures 1 and 5) within the region of large wave and mean shears occurring at this position and time. These structures become very energetic in the 2-D simulation and account for the large displacements of potential temperature and high eddy energy levels at late stages of the evolution seen in Figure 4. In the 3-D simulation the KH structures are less energetic (see Figure 7) and make their primary contributions in the $k_y \neq 0$ components of the motion field. The eddy momentum fluxes are discussed in more detail by *Fritts et al.* [this issue].

Mean Flow Evolutions

Mean velocity profiles obtained in the 2-D and 3-D simulations are displayed together in Figure 9 from $t = 40$ to 90. These show, consistent with the momentum flux profiles displayed in Figure 8, that the majority of the mean flow accelerations have occurred prior to wave dissipation by energetic instabilities ($t \sim 60$ to 70). Our purpose here is to examine the evolutions and their differences in the presence of 2-D and 3-D instabilities. The profiles are virtually indistinguishable until $t \sim 60$. Thereafter, however, the incident wave amplitudes (and momentum fluxes) begin to differ in the two simulations due to the more rapid amplitude limits imposed by the 3-D instability. The differences begin to manifest themselves in the mean velocity profiles after $t \sim 70$, where we note suppressed accelerations at greater heights and increased accelerations at lower levels in the 3-D simulation. These arise due to the greater momentum flux divergence at lower levels and the reduced fluxes at greater heights imposed by the more severe constraints on the incident wave amplitude by the 3-D instability structures.

An interesting consequence of the larger transports allowed in the 2-D simulation is the creation of a significantly larger mean shear in the 2-D than in the 3-D evolution near $z_2 \sim 0.3$ and $t \sim 70$. It is this large shear that permits the evolution of much more vigorous KH instabilities in the 2-D than in the 3-D simulation (see Figures 1 and 5). The net effect of wave and instability transports of momentum in both cases is a reduction of the initial mean shear at greater heights and enhanced shears at lower levels, with the 3-D simulation leading to generally weaker shears and a broader distribution of the momentum transported vertically from lower levels.

Summary and Conclusions

We have developed a three-dimensional, nonlinear, compressible, spectral collocation model and applied it to the problem of gravity wave breaking in the atmosphere. To facilitate efficient simulation of the wave field evolution, we chose wave parameters that would yield rapid vertical propagation and transition to instability. To demonstrate the differences between two- and three-dimensional simulations of wave instability, we have compared in this paper the two-dimensional wave field evolutions and the energetics of the wave and instability structures in two and three dimensions. Companion papers by *Fritts et al.* [this issue] and *Isler et al.* [this issue] address the detailed structure of the instability responsible for wave saturation and the subsequent transition to isotropic small-scale structure.

Our simulations reveal dramatic differences between two- and three-dimensional evolutions of a breaking gravity wave. The major differences include a very much more rapid breakdown of the unstable wave structure (within a buoyancy period), stronger constraints on wave amplitudes, and vigorous instability structures aligned parallel to the incident gravity wave in the

three-dimensional simulation (elongated in the streamwise direction), relative to the two-dimensional simulation. As a result, we conclude that wave breaking, at least in the parameter range addressed by our simulations, is an inherently three-dimensional process that cannot be described in a physical manner in two-dimensional simulations. Thus the majority of the consequences of wave breaking for the atmosphere and oceans, such as the intensity, morphology, and intermittency of turbulence, the induced transports and turbulent diffusion of heat and constituents, and the implications of wave-wave and wave-mean flow interactions for evolution of the wave spectrum with height and its influences on the mean flow, may require three-dimensional studies for their resolution. We anticipate, however, that the more important consequences of wave breaking in 3-D may be parameterized suitably in 2-D simulations once the effects are sufficiently understood.

Additional work is needed to determine whether the results presented here are representative of wave breaking for more general wave and mean flow environments. In particular, subsequent studies will address wave breaking at lower intrinsic frequencies, in more general shear flows, in a multiple-wave environment, and the implications of the induced turbulence for mixing and transports.

Acknowledgments. This research was supported by the Air Force Office of Scientific Research (AFSC) under grant F49620-92-J-0138, the SDIO/IST and managed by the Naval Research Laboratory under grant N00014-92-J-2005, and the Norwegian Defense Research Establishment. Computer resources on the CRAY Y-MP at SINTEF in Trondheim, Norway were provided by the Norwegian Ministry of Science and Education. The Norwegian Research Council for Science and Humanities (NAVF) provided travel support for Ø. Andreassen during a stay at the University of Colorado in Boulder. We also thank Ivar Lie for valuable discussions and for providing the algorithm RK2 used to advance our solutions in time and are grateful to Colin Hines and one anonymous reviewer for helpful comments on the manuscript.

References

- Andreassen, Ø., B. N. Andersen, and C. E. Wasberg, Gravity wave and convection interaction in the solar interior, *Astron. Astrophys.*, 257 (2), 763–769, 1992.
- Andreassen, Ø., I. Lie, and C. E. Wasberg, The spectral viscosity method applied to simulation of waves in a stratified atmosphere, *J. Comput. Phys.*, in press, 1993.
- Bernal, L. P. and A. Roshko, Streamwise vortex structure in plane mixing layers, *J. Fluid Mech.*, 170, 499–525, 1986.
- Breidenthal, R., Structure in turbulent mixing layers and wakes using a chemical reaction, *J. Fluid Mech.*, 109, 1–24, 1981.
- Bretherton, F. P., Momentum transfer by gravity waves, *Q. J. R. Meteorol. Soc.*, 95, 213–243, 1969.
- Browand, F. K., and T. Troutt, A note on spanwise structure in the two-dimensional mixing layer, *J. Fluid Mech.*, 97, 771–781, 1980.
- Browand, F. K., and T. Troutt, The turbulent mixing layer: Geometry of large vortices, *J. Fluid Mech.*, 158, 489–509, 1985.
- Busse, F. H., and R. M. Clever, Instabilities of convection rolls in a fluid of moderate Prandtl number, *J. Fluid Mech.*, 91, 319–335, 1979.
- Canuto, C., M. Y. Hussaini, A. Quarteroni, T. A. Zang, *Spectral Methods in Fluid Dynamics*, Springer-Verlag, New York, 1988.
- Chen, G. Q., Q. Du, and E. Tadmor, Spectral viscosity approximations to multidimensional scalar conservation laws, reprint from Univ. of Tel-Aviv, 1992.
- Clark, T. L., and R. D. Farley, Severe downslope windstorms in two and three spatial dimensions using anelastic interactive grid nesting: A possible mechanism for gustiness, *J. Atmos. Sci.*, 41, 329–350, 1984.
- Clever, R. M., and F. H. Busse, Three-dimensional convection in a horizontal fluid layer subjected to a constant shear, *J. Fluid Mech.*, 234, 511–527, 1992.
- Dunkerton, T. J., Stochastic parameterization of gravity wave stresses, *J. Atmos. Sci.*, 39, 1711–1725, 1982.
- Dunkerton, T. J., Effect of nonlinear instability on gravity wave momentum transport, *J. Atmos. Sci.*, 44, 3188–3209, 1987.
- Dunkerton, T. J., and R. E. Robins, Radiating and non-radiating modes of secondary instability in a gravity-wave critical layer, *J. Atmos. Sci.*, 49, 2546–2559, 1992.
- Fritts, D. C., The excitation of radiating waves and Kelvin-Helmholtz instabilities by the gravity wave-critical layer interaction, *J. Atmos. Sci.*, 36, 12–23, 1979.
- Fritts, D. C., The transient critical-level interaction in a Boussinesq fluid, *J. Geophys. Res.*, 87, 7997–8016, 1982.
- Fritts, D. C., A numerical study of gravity wave saturation: Nonlinear and multiple wave effects, *J. Atmos. Sci.*, 42, 2043–2058, 1985.
- Fritts, D. C., J. R. Isler, Ø. Andreassen, Gravity wave breaking in two and three dimensions, 2, Three-dimensional evolution and instability structure, *J. Geophys. Res.*, this issue.
- Garcia, R. R., and S. Solomon, The effect of the breaking gravity waves on the dynamical and chemical composition of the mesosphere and the lower thermosphere, *J. Geophys. Res.*, 90, 3850–3868, 1985.
- Hazel, P., The effect of viscosity and heat conduction on internal gravity waves at a critical level, *J. Fluid Mech.*, 30, 775–783, 1967.
- Holton, J. R., The role of gravity wave-induced drag and diffusion in the momentum budget of the mesosphere, *J. Atmos. Sci.*, 39, 791–799, 1982.
- Holton, J. R., and R. S. Lindzen, An updated theory for

- the quasi-biennial cycle of the tropical atmosphere, *J. Atmos. Sci.*, 29, 1076–1080, 1972.
- Huang, C. M., F. S. Kuo, H. Y. Lue, C. H. Liu, Numerical simulations of the saturated gravity wave spectra in the atmosphere, *J. Atmos. Terr. Phys.*, 54, 129–142, 1992.
- Isler, J. R., D. C. Fritts, and Ø. Andreassen, Gravity wave breaking in two and three dimensions, 3, Vortex breakdown and transition to isotropy, *J. Geophys. Res.*, this issue.
- Jimenez, J., A spanwise structure in the plane shear layer, *J. Fluid Mech.*, 132, 319–336, 1983.
- Klassen, G. P., and W. R. Peltier, The onset of turbulence in finite amplitude Kelvin-Helmholtz billows, *J. Fluid Mech.*, 34, 609–624, 1985.
- Landau, L. D., and E. M. Lifshitz, *Fluid Dynamics*, Pergamon, New York, 1959.
- Lasheras, J. C., J. S. Cho, and T. Maxworthy, On the origin and evolution of streamwise vortical structures in a plane, free shear layer, *J. Fluid Mech.*, 172, 231–258, 1986.
- Maday, Y., and E. Tadmor, Analysis of the spectral viscosity method for periodic conservation laws, *SIAM J. Numer. Anal.*, 26, 854–870, 1989.
- Maday, Y., S. M. O. Kaber, and E. Tadmor, Legendre pseudospectral viscosity method for nonlinear conservation laws, *SIAM J. Numer. Anal.*, in press, 1993.
- McFarlane, N. A., The effect of orographically excited gravity wave drag on the general circulation of the lower stratosphere and troposphere, *J. Atmos. Sci.*, 44, 1775–1800, 1987.
- McIntyre, M. E., On dynamics and transport near the polar mesopause in summer, *J. Geophys. Res.*, 94, 14617–14628, 1989.
- Metcalfe, R. W., S. A. Orszag, M. E. Brachet, S. Menon, and J. J. Riley, Secondary instability of a temporally growing mixing layer, *J. Fluid Mech.*, 184, 207–243, 1987.
- Nagata, M., and F. H. Busse, Three-dimensional tertiary motions in a plane shear layer, *J. Fluid Mech.*, 135, 1–26, 1983.
- Palmer, T. N., G. J. Shutts, and R. Swinbank, Alleviation of the systematic westerly bias in general circulation and numerical weather prediction models through an orographic gravity wave drag parameterization, *Q. J. R. Meteorol. Soc.*, 112, 1001–1040, 1986.
- Pierrehumbert, R. T., and S. E. Widnall, The two- and three-dimensional instabilities of a spatially periodic shear layer, *J. Fluid Mech.*, 114, 59–82, 1982.
- Tadmor, E., Convergence of spectral methods for nonlinear conservation laws, *SIAM J. Numer. Anal.*, 26, 30–44, 1989.
- Walterscheid, R. L., and J. Schubert, Nonlinear evolution of an upward propagating gravity wave: overturning, convection, transience and turbulence, *J. Atmos. Sci.*, 47, 101–125, 1990.
- Wasberg, C. E., On the Chebyshev collocation approximation and domain decomposition, *Tech. Rep. FFI/Rapp.-92/7092*, Norw. Def. Res. Estab., Kjeller Norway, 1992.
- Wasberg, C. E., and Ø. Andreassen, Pseudospectral methods with open boundary conditions for the study of atmospheric wave phenomena, *Comput. Methods Appl. Mech. Eng.*, 80, 459–465, 1990.
- Winters, K. B., and E. A. D'Asaro, Two-dimensional instability of finite amplitude internal gravity wave packets near a critical level, *J. Geophys. Res.*, 94, 12,709–12,719, 1989.
- Winters, K. B., and E. A. D'Asaro, 3D wave breaking near a critical level, *J. Fluid Mech.*, in press, 1993.
- Winters, K. B., and J. Riley, Instability of internal waves near a critical level, *Dyn. Atmos. Oceans*, 16, 249–278, 1992.

Ø. Andreassen and C. E. Wasberg, Norwegian Defense Research Establishment, P. O. Box 25, N-2007, Kjeller, Norway.

D. C. Fritts and J. R. Isler, Laboratory for Atmospheric and Space Physics and Department of Electrical and Computer Engineering, Campus Box 425, University of Colorado, Boulder, CO 80309.

(Received April 1, 1993; revised December 1, 1993; accepted December 1, 1993.)